Supplemental Material for Dissipationless counterflow above T_c in bilayer superconductors

Guido Homann,[1] Marios H. Michael,[2] Jayson G. Cosme,[3] and Ludwig Mathey[4,5]

[1] *Zentrum für Optische Quantentechnologien and Institut für Quantenphysik, Universität Hamburg, 22761 Hamburg, Germany*
[2] *Max Planck Institute for the Structure and Dynamics of Matter, Luruper Chausse 149, 22761 Hamburg, Germany*
[3] *National Institute of Physics, University of the Philippines, Diliman, Quezon City 1101, Philippines*
[4] *Zentrum für Optische Quantentechnologien and Institut für Laserphysik, Universität Hamburg, 22761 Hamburg, Germany*
[5] *The Hamburg Centre for Ultrafast Imaging, Luruper Chaussee 149, 22761 Hamburg, Germany*

CONTENTS

I. LAGRANGIAN AND EQUATIONS OF MOTION

Here, we present our semiclassical $U(1)$ lattice gauge theory [1–3] in detail. The in-plane lattice constant $d_{x,\mathbf{r}} = d_{y,\mathbf{r}} = d_{ab}$ is introduced as a short-range cutoff below the in-plane coherence length. The interlayer distances are $d_{z,\mathbf{r}} = d_s$ for intrabilayer (strong) junctions and $d_{z,\mathbf{r}} = d_w$ for interbilayer (weak) junctions, reproducing the spacing of CuO_2 planes in the crystal. The Lagrangian of the lattice gauge model consists of three terms,

$$\mathcal{L} = \mathcal{L}_{\rm sc} + \mathcal{L}_{\rm em} + \mathcal{L}_{\rm kin}. \tag{1}$$

The first term is the $|\psi|^4$ model of the superconducting condensate in the absence of Cooper pair tunneling,

$$\mathcal{L}_{\rm sc} = \sum_{\mathbf{r}} K\hbar^2|\partial_t\psi_{\mathbf{r}}|^2 + \mu|\psi_{\mathbf{r}}|^2 - \frac{g}{2}|\psi_{\mathbf{r}}|^4, \tag{2}$$

where the Ginzburg-Landau coefficients μ and g are kept fixed throughout this work. The coefficient K is related to the Thomas-Fermi screening length $\lambda_{\rm TF}$ [4], $K = \epsilon_0/8e^2|\psi_0|^2\lambda_{\rm TF}^2$. We formulate the Lagrangian of the free electromagnetic field on an anisotropic lattice,

$$\mathcal{L}_{\rm em} = \sum_{j,\mathbf{r}} \frac{\kappa_{j,\mathbf{r}}\epsilon_\infty\epsilon_0}{2}E_{j,\mathbf{r}}^2 - \frac{\kappa_{z,\mathbf{r}}}{\kappa_{j,\mathbf{r}}\beta_{j,\mathbf{r}}^2\mu_0}\Big[1-\cos\big(\beta_{j,\mathbf{r}}B_{j,\mathbf{r}}\big)\Big]. \tag{3}$$

We employ the temporal gauge, where the electric field is given by the time derivative of the vector potential, $E_{j,\mathbf{r}} = -\partial_t A_{j,\mathbf{r}}$. The j component of the electric field lies on the bond from site $\mathbf{r}$ to its nearest neighbor in the $j \in \{x,y,z\}$ direction. The magnetic field components $B_{j,\mathbf{r}} = \epsilon_{jkl}\delta_k A_{l,\mathbf{r}}$ are centered on the plaquettes of the lattice. We calculate the spatial derivatives according to $\delta_k A_{l,\mathbf{r}} = (A_{l,\mathbf{r}+\mathbf{u}_k} - A_{l,\mathbf{r}})/d_{l,\mathbf{r}}$, where $\mathbf{u}_k$ is the unit vector in the k direction. The background permittivity ϵ_∞ is due to bound charges. The other prefactors in Eq. (3) are linked to the anisotropic lattice geometry. Introducing $d_c = (d_s + d_w)/2$, we write $\kappa_{x,\mathbf{r}} = \kappa_{y,\mathbf{r}} = 1$ and $\kappa_{z,\mathbf{r}} = d_{z,\mathbf{r}}/d_c$, while $\beta_{x,\mathbf{r}} = \beta_{y,\mathbf{r}} = 2ed_{ab}d_{z,\mathbf{r}}/\hbar$ and $\beta_{z,\mathbf{r}} = 2ed_{ab}^2/\hbar$. The kinetic part of the Lagrangian,

$$\mathcal{L}_{\rm kin} = -\sum_{j,\mathbf{r}} t_{j,\mathbf{r}}|\psi_{\mathbf{r}+\mathbf{u}_j} - \psi_{\mathbf{r}}e^{ia_{j,\mathbf{r}}}|^2, \tag{4}$$

accounts for nearest-neighbor tunneling of Cooper pairs. The unitless vector potential $a_{j,\mathbf{r}} = -2ed_{j,\mathbf{r}}A_{j,\mathbf{r}}/\hbar$ couples to the phase of the order parameter, ensuring the local gauge-invariance of $\mathcal{L}_{\rm kin}$. This coupling reflects the Coulomb interaction between the Cooper pairs. The tunneling coefficients are $t_{x,\mathbf{r}} = t_{y,\mathbf{r}} = t_{ab}$ for in-plane junctions, $t_{z,\mathbf{r}} = t_s$ for intrabilayer junctions, and $t_{z,\mathbf{r}} = t_w$ for interbilayer junctions.

The equations of motion read

$$\partial_t^2\psi_{\mathbf{r}} = \frac{1}{K\hbar^2}\frac{\partial\mathcal{L}}{\partial\psi_{\mathbf{r}}^*} - \gamma_{\rm sc}\partial_t\psi_{\mathbf{r}} + \xi_{\mathbf{r}}, \tag{5}$$

$$\partial_t^2 A_{j,\mathbf{r}} = \frac{1}{\epsilon_\infty\epsilon_0}\frac{\partial\mathcal{L}}{\partial A_{j,\mathbf{r}}} - \gamma_{j,\mathbf{r}}\partial_t A_{j,\mathbf{r}} + \eta_{j,\mathbf{r}}, \tag{6}$$

where $\gamma_{\rm sc}$ and $\gamma_{j,\mathbf{r}}$ are phenomenological damping constants of the superconducting order parameter and the vector potential, respectively. The damping constants of the vector potential are $\gamma_{x,\mathbf{r}} = \gamma_{y,\mathbf{r}} = \gamma_{ab}$ for in-plane junctions, $\gamma_{z,\mathbf{r}} = \gamma_s$ for intrabilayer junctions, and $\gamma_{z,\mathbf{r}} = \gamma_w$ for interbilayer junctions. The Langevin noise terms $\xi_{\mathbf{r}}$ and $\boldsymbol{\eta}_{\mathbf{r}}$ have a white Gaussian distribution with zero mean. To satisfy the fluctuation-dissipation theorem, we take the noise of the order parameter as

$$\langle{\rm Re}\{\xi_{\mathbf{r}}(t)\}{\rm Re}\{\xi_{\mathbf{r}'}(t')\}\rangle = \frac{\gamma_{\rm sc}k_{\rm B}T}{K\hbar^2V_0}\delta_{\mathbf{r}\mathbf{r}'}\delta(t-t')\,, \tag{7}$$

$$\langle{\rm Im}\{\xi_{\mathbf{r}}(t)\}{\rm Im}\{\xi_{\mathbf{r}'}(t')\}\rangle = \frac{\gamma_{\rm sc}k_{\rm B}T}{K\hbar^2V_0}\delta_{\mathbf{r}\mathbf{r}'}\delta(t-t')\,, \tag{8}$$

$$\langle{\rm Re}\{\xi_{\mathbf{r}}(t)\}{\rm Im}\{\xi_{\mathbf{r}'}(t')\}\rangle = 0, \tag{9}$$

where $V_0 = d_{ab}^2 d_c$. The noise correlations for the vector potential are

$$\langle\eta_{x,\mathbf{r}}(t)\eta_{x,\mathbf{r}'}(t')\rangle = \frac{2\gamma_{ab}k_{\rm B}T}{\epsilon_\infty\epsilon_0V_0}\delta_{\mathbf{r}\mathbf{r}'}\delta(t-t'), \tag{10}$$

$$\langle\eta_{y,\mathbf{r}}(t)\eta_{y,\mathbf{r}'}(t')\rangle = \frac{2\gamma_{ab}k_{\rm B}T}{\epsilon_\infty\epsilon_0V_0}\delta_{\mathbf{r}\mathbf{r}'}\delta(t-t'), \tag{11}$$

$$\langle\eta_{z,\mathbf{r}}(t)\eta_{z,\mathbf{r}'}(t')\rangle = \frac{2\gamma_{z,\mathbf{r}}k_{\rm B}T}{\kappa_{z,\mathbf{r}}\epsilon_\infty\epsilon_0V_0}\delta_{\mathbf{r}\mathbf{r}'}\delta(t-t'). \tag{12}$$

II. MODEL PARAMETERS

We simulate a bilayer cuprate with $N = 40 \times 40 \times 4$ lattice sites. The model parameters are specified in Table I.

TABLE I. Model parameters of the simulated bilayer cuprate.

K (meV^{-1})	2.9×10^{-5}
μ (meV)	1.0×10^{-2}
g (meV Å^3)	5.0
ϵ_∞	4
d_{ab} (Å)	15
d_s (Å)	4
d_w (Å)	8
t_{ab} (meV)	5.7×10^{-1}
t_s (meV)	3.9×10^{-2}
t_w (meV)	3.6×10^{-4}
$\gamma_{\rm H}/2\pi$ (THz)	1.0
$\gamma_{ab}/2\pi$ (THz)	7.0
$\gamma_s/2\pi$ (THz)	1.2
$\gamma_w/2\pi$ (THz)	0.4

III. PLASMA RESONANCES

A bilayer superconductor has two longitudinal Josephson plasma modes, which govern the dynamics of the Cooper pairs along the c axis. The ground state expressions [5, 6] for the two Josephson plasma frequencies are

$$\omega^2_{\rm J1,J2} = \left(\frac{1}{2}+\alpha_s\right)\Omega_s^2 + \left(\frac{1}{2}+\alpha_w\right)\Omega_w^2 \mp \sqrt{\left[\left(\frac{1}{2}+\alpha_s\right)\Omega_s^2 - \left(\frac{1}{2}+\alpha_w\right)\Omega_w^2\right]^2 + 4\alpha_s\alpha_w\Omega_s^2\Omega_w^2}. \tag{13}$$

The bare plasma frequencies of the interlayer junctions are given by

$$\Omega_{s,w} = \sqrt{\frac{8t_{s,w}|\psi_0|^2e^2d_cd_{s,w}}{\epsilon_\infty\epsilon_0\hbar^2}}, \tag{14}$$

and the capacitive coupling constants [4, 7, 8] are

$$\alpha_{s,w} = \frac{\epsilon_\infty\epsilon_0}{8K|\psi_0|^2e^2d_cd_{s,w}}, \tag{15}$$

where $d_c = (d_s+d_w)/2$ is the average c-axis spacing. The parameter choice in Table I implies $\alpha_w \approx 1$, and $\alpha_s \approx 2$. The bare plasma frequencies are $\Omega_w/2\pi \approx 0.9$ THz and $\Omega_s/2\pi \approx 6.3$ THz, resulting in the Josephson plasma frequencies

$$\omega_{\rm J1} \approx 2\pi \times 1.0 \text{ THz}, \tag{16}$$

$$\omega_{\rm J2} \approx \Omega_s\sqrt{1+2\alpha_s} \approx 2\pi \times 14.1 \text{ THz}. \tag{17}$$

To study the temperature dependence of the Josephson plasma modes, we compute the power spectra of the interlayer supercurrents based on an ensemble of 1000 trajectories. The Josephson current along a single junction in the z direction is given by

$$J^z_{l,m,n} = \frac{2et_{z,\mathbf{r}}d_c}{i\hbar}\left(\psi^*_{l,m,n+1}\psi_{l,m,n}e^{ia^z_{l,m,n}} - c.c.\right). \tag{18}$$

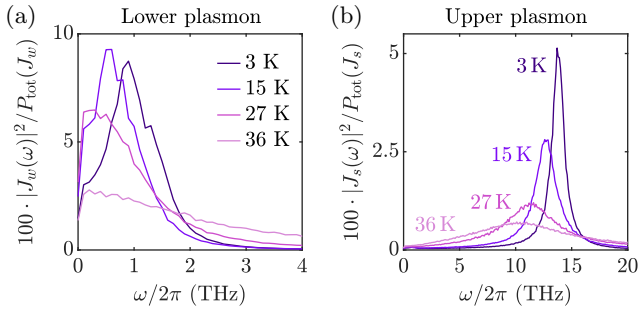

FIG. 1. Thermal distribution of the interlayer currents. (a) Power spectrum of the interbilayer current at different temperatures. (b) Power spectrum of the intrabilayer current at different temperatures. Each spectrum is based on an ensemble average of 1000 trajectories, and the spectral power is normalized by the total power. The crossover temperature is $T_c \sim 25$ K.

For each trajectory, we record the average interbilayer supercurrent

$$J_w = \frac{1}{N_{xy}} \sum_{l,m} J^z_{l,m,2} \tag{19}$$

and the average intrabilayer supercurrent

$$J_s = \frac{1}{N_{xy}} \sum_{l,m} J^z_{l,m,1} \tag{20}$$

over a time interval of 10 ps. We then compute the Fourier transforms $J_{w,s}(\omega)$ and evaluate the ensemble averages $\langle |J_{w,s}(\omega)|^2 \rangle$. One can see in Fig. 1(a) that the lower Josephson plasma resonance shifts to lower frequencies with increasing temperature and vanishes around T_c. This is also observed in experiments [9, 10].

As shown in Fig. 1(b), the upper Josephson plasma resonance broadens with increasing temperature and shifts to lower frequencies. The latter is also visible in Fig. 2(a), where the peak frequency $\omega_{s,\rm peak}$ is displayed as a function of temperature. We compare the peak frequency to the thermal average

$$\omega_{\rm J2,th} = \Omega_s \sqrt{\frac{\langle C^s_{l,m} \rangle}{|\psi_0|^2} + \alpha_s \left\langle \frac{C^s_{l,m}}{|\psi_{l,m,1}|^2} + \frac{C^s_{l,m}}{|\psi_{l,m,2}|^2} \right\rangle}, \tag{21}$$

where

$$C^s_{l,m} = \frac{1}{2} \left(\psi^*_{l,m,2} \psi_{l,m,1} e^{i a^z_{l,m,1}} + c.c. \right). \tag{22}$$

This simple estimate describes the average renormalization of the plasma frequency of the intrabilayer junctions. It accounts for the renormalization of both the effective intrabilayer tunneling and the order parameter due to thermal fluctuations. At temperatures above 20 K, $\omega_{\rm J2,th}$ is clearly smaller than $\omega_{s,\rm peak}$. Remarkably, the discrepancy

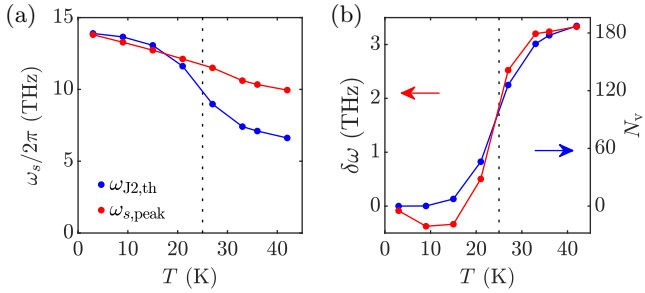

FIG. 2. Temperature dependence of the upper Josephson plasma resonance. (a) Temperature dependence of the peak frequency and the thermal average of the upper Josephson plasma frequency. (b) The discrepancy $\delta\omega = \omega_{s,\rm peak} - \omega_{\rm J2,th}$ has a similar temperature dependence as the number of vortices per layer $N_{\rm v}$. The crossover temperature is $T_c \sim 25$ K.

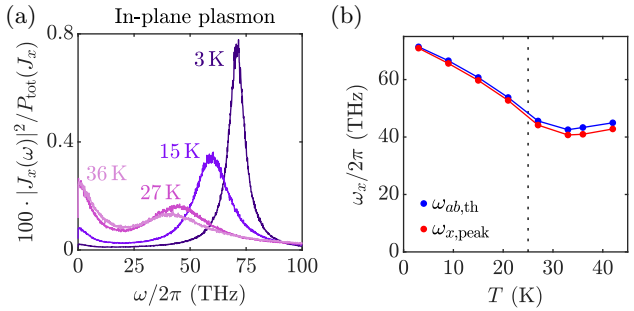

FIG. 3. Temperature dependence of the in-plane plasma resonance. (a) Power spectrum of the in-plane currents at different temperatures. Each spectrum is based on an ensemble average of 1000 trajectories, and the spectral power is normalized by the total power. (b) Temperature dependence of the peak frequency and the thermal average of the in-plane plasma frequency. The crossover temperature is $T_c \sim 25$ K.

$\delta\omega = \omega_{s,\rm peak} - \omega_{\rm J2,th}$ follows a similar temperature dependence as the areal density of vortices, which is highlighted by Fig. 2(b). This indicates that the appearance of vortices leads to a significant stabilization of the upper Josephson plasma frequency.

We now turn to the temperature dependence of the in-plane plasma frequency. At zero temperature, the in-plane plasma frequency is

$$\omega_{ab} = \sqrt{\frac{8t_{ab}|\psi_0|^2e^2d_{ab}^2}{\epsilon_\infty\epsilon_0\hbar^2}} \approx 2\pi \times 73.7 \text{ THz}. \tag{23}$$

We evaluate the average supercurrent along the x axis based on the definition

$$J_x = \frac{1}{2N_{xy}}\sum_{l,m}\sum_{n=1}^{2} J^x_{l,m,n}, \tag{24}$$

where

$$J^x_{l,m,n} = \frac{2et_{ab}d_{ab}}{i\hbar}\left(\psi^*_{l+1,m,n}\psi_{l,m,n}e^{ia^x_{l,m,n}} - c.c.\right). \tag{25}$$

In Fig. 3(a), we present the power spectrum of the supercurrents along the x axis at different temperatures. Similarly to the upper Josephson plasma resonance, the in-plane plasma resonance broadens with increasing temperature. While the peak frequency $\omega_{x,\rm peak}$ decreases monotonically with increasing temperature below T_c, it slowly increases above T_c. This behavior is consistent with the temperature dependence of the order parameter. Indeed, we find that the temperature dependence of $\omega_{x,\rm peak}$ is described by the average renormalization of the plasma frequency of the in-plane junctions. As evidenced by Fig. 3(b), $\omega_{x,\rm peak}$ is in good agreement with the thermal average

$$\omega_{ab,\rm th} = \omega_{ab}\sqrt{\frac{\langle\psi^*_{l+1,m,n}\psi_{l,m,n}e^{ia^x_{l,m,n}} + c.c.\rangle}{2|\psi_0|^2}} \tag{26}$$

at all simulated temperatures.

IV. TEMPERATURE DEPENDENCE OF THE IN-PLANE TUNNELING AND THE SUPERCONDUCTING ORDER PARAMETER

In this section, we show the behavior of the effective in-plane tunneling coefficient and the amplitude of the order parameter across the phase ordering transition described in the main text.

The temperature dependence of the effective in-plane tunneling coefficient $t_{ab,\rm eff} = t_{ab}\langle\cos\theta^x_{\mathbf{r}}\rangle$ is plotted in Fig. 4(a). Local phase fluctuations reduce the effective in-plane tunneling coefficient through disorder averaging of $\langle\cos\theta^x_{\mathbf{r}}\rangle$.

The temperature dependence of the order parameter is displayed in Fig. 4(b). In the ground state at $T = 0$, the amplitude of the order parameter is given by $|\psi_0|^2 = \mu/g = 2\times10^{21}$ cm^{-3}. The order parameter first decreases with

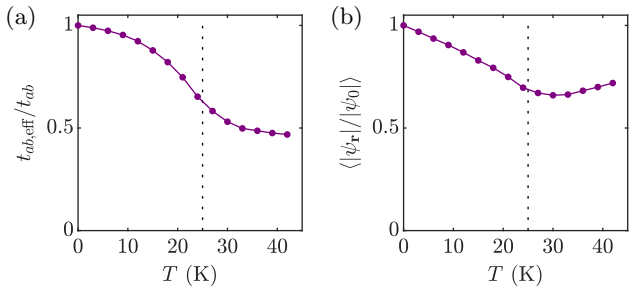

FIG. 4. Temperature dependence of the in-plane tunneling and the superconducting order parameter. (a) Temperature dependence of the effective in-plane tunneling coefficient. (b) Temperature dependence of the amplitude of the order parameter. Both quantities are averaged over all lattice sites, a time interval of 2 ps (200 measurements), and an ensemble of 100 trajectories. The standard error of each data point is comparable to the point size. The crossover temperature is $T_c \sim 25$ K.

increasing temperature and reaches a minimum of $\langle|\psi_{\mathbf{r}}|\rangle/|\psi_0| \approx 0.66$ around 30 K. Above 30 K, it slowly increases with increasing temperature. This behavior is consistent with an order-disorder transition [11]. We attribute the temperature dependence of the order parameter to a modification of the order parameter potential due to phase fluctuations, depleting the order parameter at temperatures below 30 K. However, as temperature is further increased, amplitude fluctuations are also strongly excited, leading to an increase of $\langle|\psi_{\mathbf{r}}|\rangle$.

V. VORTEX CORRELATIONS

Using the definition for the vorticity given by Eq. (4) in the main text, we define the two-point correlation function of vortices in the xy plane,

$$V_{ab}(x_i, y_j, t) = \frac{\langle v_{l,m,n}(0) v_{l+i,m+j,n}(t)\rangle}{\langle v^2_{l,m,n}(0)\rangle}. \tag{27}$$

In Fig. 5(a), we show the equal-time in-plane vortex correlation function at 36 K. It reveals a strong tendency to the formation of vortex-antivortex pairs. The accumulated probability to find an antivortex on the nearest or next-nearest plaquettes of a vortex amounts to 94%. On larger length scales, in-plane vortex correlations are negligible. Next, we consider the cumulative correlation function

$$V_{ab}(r, t) = \sum_{|(x_i,y_j)|=r} V_{ab}(x_i, y_j, t), \tag{28}$$

where the sum is taken over all (x_i, y_j) with $x_i^2 + y_j^2 = r^2$. One can see in Fig. 5(b) that vortex-antivortex pairs annihilate on a time scale of a few femtoseconds.

In Fig. 5(c), we show the relative amount of isolated vortices as a function of temperature. An isolated vortex is a vortex without an vortex of opposite vorticity on the nearest or next-nearest neighbor plaquettes. The percentage of isolated vortices grows below T_c and saturates at higher temperature. This indicates a transition from bound to unbound vortices akin to a Kosterlitz-Thouless transition. The percentage of isolated vortices is limited by the areal density of vortices.

Furthermore, we calculate the interlayer correlation functions

$$V_s = \frac{\langle \tilde{v}_{l,m,1} \tilde{v}_{l,m,2}\rangle}{\langle \tilde{v}^2_{l,m,n}\rangle}, \tag{29}$$

$$V_w = \frac{\langle \tilde{v}_{l,m,2} \tilde{v}_{l,m,3}\rangle}{\langle \tilde{v}^2_{l,m,n}\rangle}, \tag{30}$$

where

$$\tilde{v}_{l,m,n} = \sum_{l'=l-1}^{l+1} \sum_{m'=m-1}^{m+1} v_{l',m',n} \tag{31}$$

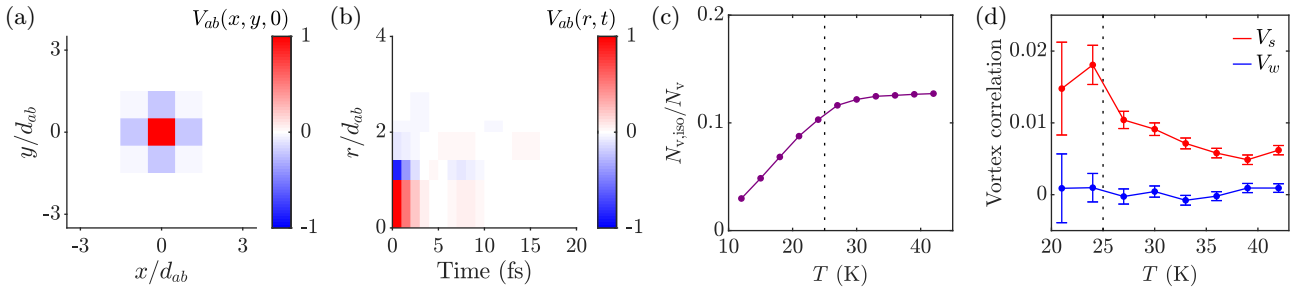

FIG. 5. Vortex excitations. (a) Equal-time in-plane vortex correlation function at 36 K $\sim 1.4T_c$. (b) Time-resolved in-plane vortex correlation function at 36 K, where $r^2 = x^2 + y^2$. (c) Relative amount of isolated vortices at different temperatures. Isolated vortices are vortices without an antivortex on the nearest or next-nearest neighbor plaquettes. (d) Interlayer vortex correlations. The results in (a) and (b) are obtained from an ensemble average of 1000 trajectories. Each data point in (c) and (d) is based on an ensemble average of 100 trajectories.

is the vorticity of a bin of 9 plaquettes. The interlayer vortex correlation functions are displayed in Fig. 5(d). While interbilayer vortex correlations are generally negligible, intrabilayer vortex correlations are larger than zero at all simulated temperatures. The intrabilayer correlations are small and follow a similar temperature dependence as the effective intrabilayer coupling; see Fig. 2(b) in the main text. Note that the in-plane penetration depth $\lambda_{ab} = \omega_{ab}/c\sqrt{\epsilon_\infty} \approx 324$ nm is larger than the in-plane system size of 60 nm.

VI. CORRELATIONS OF THE INTRABILAYER JOSEPHSON POTENTIAL

In the presence of fluctuating vortices, the intrabilayer Josephson potential becomes disordered and fluctuating. We characterize this effect by computing the power spectra of spatial and time variations around the spatiotemporal mean, through the function

$$F(\mathbf{r},t) = \cos\theta_s(\mathbf{r},t) - \langle\cos\theta_s(\mathbf{r},t)\rangle. \tag{32}$$

For each trajectory of an ensemble of 1000 trajectories, we record $F(\mathbf{r},t)$ for 2 ps with a detection rate of 5 PHz and compute the Fourier transform

$$F(\mathbf{k},\omega) = \frac{1}{N_t}\sum_{\mathbf{r}}\sum_{j} F(\mathbf{r},t_j)\, e^{i(\mathbf{k}\cdot\mathbf{r}-\omega t_j)}, \tag{33}$$

where $N_t = 10^4$ is the number of measurements per trajectory. In Fig. 6, we show a selection of power spectra $|F(\mathbf{k},\omega)|^2$, based on the ensemble average of 1000 trajectories. Note that $F(\mathbf{k}=0,\omega=0) = 0$. We find that the disordered potential is peaked at the lowest momenta. As a function of frequency, we see noisy dynamics with fluctuations up to ~ 5 THz.

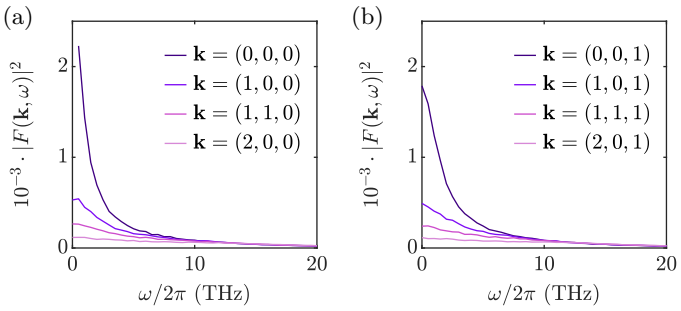

FIG. 6. Power spectra of the disorder function at 36 K $\sim 1.4T_c$. (a) Power spectra of the disorder function for various momenta with $k_z = 0$. (b) Power spectra of the disorder function for various momenta with $k_z = \pi/2d_c$. The in-plane momentum components are specified in units of $2\pi/L_{ab}$. The power spectra are evaluated from an ensemble average of 1000 trajectories.

VII. DETAILS ON THE CONDUCTIVITY MEASUREMENTS

In the main text, we present numerical results for the symmetric and antisymmetric components of the in-plane conductivity. To measure the symmetric conductivity σ_+, we add a spatially homogeneous probe current to the equations of motion for $A_{x,\mathbf{r}}$,

$$\partial_t^2 A^x_{l,m,n} = \frac{1}{\epsilon_\infty \epsilon_0} \frac{\partial \mathcal{L}}{\partial A^x_{l,m,n}} - \gamma_{ab} \partial_t A^x_{l,m,n} + \eta^x_{l,m,n} - \frac{J_{\mathrm{sym}}}{\epsilon_\infty \epsilon_0} \cos(\omega_{\mathrm{pr}} t). \tag{34}$$

Once a steady state is reached, we record the symmetric component of the electric field

$$E_+ = \frac{1}{N} \sum_{l,m,n} E^x_{l,m,n} = \frac{1}{N} \sum_{l,m,n} \left(-\partial_t A^x_{l,m,n} \right) \tag{35}$$

and the symmetric component of the current

$$J_+ = \frac{1}{N_z} \sum_n J^x_n. \tag{36}$$

The average current J^x_n in layer n includes superconducting, normal and capacitive contributions,

$$J^x_n = J^x_{n,\mathrm{sup}} + J^x_{n,\mathrm{nor}} + J^x_{n,\mathrm{cap}}. \tag{37}$$

The superconducting current is given by

$$J^x_{n,\mathrm{sup}} = \frac{1}{N_{xy}} \sum_{l,m} \frac{2e t_{ab} d_{ab}}{i\hbar} \left(\psi^*_{l+1,m,n} \psi_{l,m,n} e^{i a^x_{l,m,n}} - c.c. \right). \tag{38}$$

The normal current is given by

$$J^x_{n,\mathrm{nor}} = \frac{1}{N_{xy}} \sum_{l,m} \epsilon_\infty \epsilon_0 \gamma_{ab} E^x_{l,m,n}. \tag{39}$$

The capacitive current is given by

$$J^x_{n,\mathrm{cap}} = \frac{1}{N_{xy}} \sum_{l,m} \epsilon_\infty \epsilon_0 \partial_t E^x_{l,m,n}. \tag{40}$$

For $\omega_{\mathrm{pr}}/2\pi = 1$ THz, we record $E_+(t)$ and $J_+(t)$ for 20 ps. For all other probe frequencies, we record $E_+(t)$ and $J_+(t)$ for 4 ps. Following this protocol, we evaluate $\sigma_+(\omega_{\mathrm{pr}}) = J_+(\omega_{\mathrm{pr}})/E_+(\omega_{\mathrm{pr}})$ for 100–1000 trajectories and take the ensemble average. We use $J_{\mathrm{sym}} = 500\ \mathrm{kA\,cm^{-2}}$. Thus, we probe the linear response as evidenced by Fig. 7.

To measure the antisymmetric conductivity σ_-, we proceed analogously to the symmetric case. Here, the probe current alternates from layer to layer, i.e.,

$$\partial_t^2 A^x_{l,m,n} = \frac{1}{\epsilon_\infty \epsilon_0} \frac{\partial \mathcal{L}}{\partial A^x_{l,m,n}} - \gamma_{ab} \partial_t A^x_{l,m,n} + \eta^x_{l,m,n} - \frac{(-1)^n J_{\mathrm{asym}}}{\epsilon_\infty \epsilon_0} \cos(\omega_{\mathrm{pr}} t). \tag{41}$$

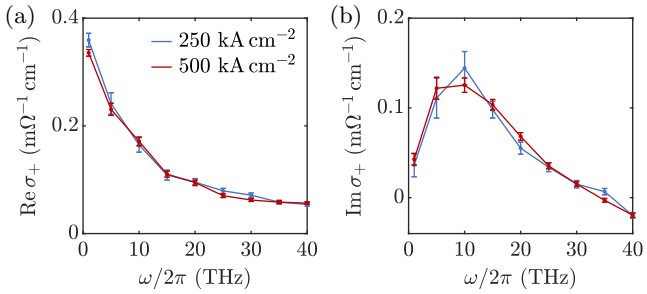

FIG. 7. Symmetric conductivity for different probe strengths at 36 K $\sim 1.4T_c$. (a) Real part. (b) Imaginary part. The error bars indicate the standard errors of the ensemble averages.

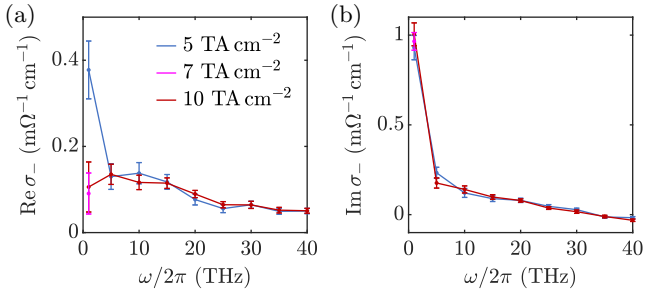

FIG. 8. Antisymmetric conductivity for different probe strengths at 36 K $\sim 1.4T_c$. (a) Real part. (b) Imaginary part. The error bars indicate the standard errors of the ensemble averages.

Once a steady state is reached, we record the antisymmetric component of the electric field

$$E_- = \frac{1}{N}\sum_{l,m,n}(-1)^n E^x_{l,m,n} \tag{42}$$

and the antisymmetric component of the current

$$J_- = \frac{1}{N_z}\sum_{n}(-1)^n J^x_n. \tag{43}$$

For $\omega_{\rm pr}/2\pi = 1$ THz, we record $E_+(t)$ and $J_+(t)$ for 20 ps. For all other probe frequencies, we record $E_+(t)$ and $J_+(t)$ for 4 ps. Following this protocol, we evaluate $\sigma_-(\omega_{\rm pr}) = J_-(\omega_{\rm pr})/E_-(\omega_{\rm pr})$ for 100–1000 trajectories and take the ensemble average. In Fig. 8, we show data for probe strengths of $J_{\rm asym} = 5\times10^9$ kA cm^{-2}, $J_{\rm asym} = 7\times10^9$ kA cm^{-2}, and $J_{\rm asym} = 10^{10}$ kA cm^{-2}. We suspect that the measurement with $J_{\rm asym} = 5\times10^9$ kA cm^{-2} at 1 THz is poorly converged and use the data from the measurement with $J_{\rm asym} = 7\times10^9$ kA cm^{-2} in the main text. For all other probe strengths, we use the results from the measurements with $J_{\rm asym} = 5\times10^9$ kA cm^{-2}. Note that $J_{\rm asym}$ is significantly larger than $J_{\rm sym}$ because the antisymmetric probe current induces a magnetic field that strongly screens the antisymmetric current.

Furthermore, we measure the symmetric and antisymmetric conductivity for a z-axis momentum of $k_z = \pi/2d_c$. The corresponding current configurations are depicted in Fig. 9(a). One can see in Figs. 9(b) and 9(c) that σ_+ and σ_- have no significant dependence on k_z. This confirms that the interbilayer coupling between vortices is negligible as indicated by Fig. 5(d).

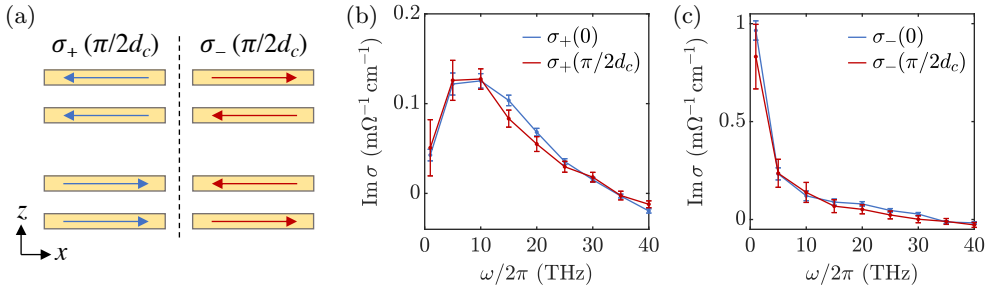

FIG. 9. Dependence of the symmetric and antisymmetric conductivity on the z-axis momentum. (a) Current configurations characterized by the symmetric and antisymmetric conductivity, respectively, for $k_z = \pi/2d_c$. (b) Imaginary part of σ_+ for $k_z = 0$ and $k_z = \pi/2d_c$ at 36 K $\sim 1.4T_c$. (c) Imaginary part of σ_- for $k_z = 0$ and $k_z = \pi/2d_c$ at 36 K. The error bars indicate the standard errors of the ensemble averages.

[1] G. Homann, J. G. Cosme, and L. Mathey, Higgs time crystal in a high-T_c superconductor, Phys. Rev. Research **2**, 043214 (2020).

[2] G. Homann, J. G. Cosme, J. Okamoto, and L. Mathey, Higgs mode mediated enhancement of interlayer transport in high-T_c cuprate superconductors, Phys. Rev. B **103**, 224503 (2021).

[3] G. Homann, J. G. Cosme, and L. Mathey, Parametric control of Meissner screening in light-driven superconductors, New J. Phys. **24**, 113007 (2022).

[4] M. Machida, T. Koyama, and M. Tachiki, Dynamical breaking of charge neutrality in intrinsic Josephson junctions: Common origin for microwave resonant absorptions and multiple-branch structures in the $I - V$ characteristics, Phys. Rev. Lett. **83**, 4618 (1999).

[5] D. van der Marel and A. A. Tsvetkov, Transverse-optical Josephson plasmons: Equations of motion, Phys. Rev. B **64**, 024530 (2001).

[6] T. Koyama, Josephson plasma resonances and optical properties in high-T_c superconductors with alternating junction parameters, J. Phys. Soc. Jpn. **71**, 2986 (2002).

[7] T. Koyama and M. Tachiki, I-V characteristics of Josephson-coupled layered superconductors with longitudinal plasma excitations, Phys. Rev. B **54**, 16183 (1996).

[8] M. Machida and T. Koyama, Localized rotating-modes in capacitively coupled intrinsic Josephson junctions: Systematic study of branching structure and collective dynamical instability, Phys. Rev. B **70**, 024523 (2004).

[9] H. Shibata and T. Yamada, Double Josephson plasma resonance in T^* phase $SmLa_{1-x}Sr_xCuO_{4-\delta}$, Phys. Rev. Lett. **81**, 3519 (1998).

[10] A. von Hoegen, M. Fechner, M. Först, N. Taherian, E. Rowe, A. Ribak, J. Porras, B. Keimer, M. Michael, E. Demler, and A. Cavalleri, Amplification of superconducting fluctuations in driven $YBa_2Cu_3O_{6+x}$, Phys. Rev. X **12**, 031008 (2022).

[11] T. Schneider and E. Stoll, Molecular-dynamics study of structural-phase transitions. I. One-component displacement models, Phys. Rev. B **13**, 1216 (1976).